IEEE Access
Multidisciplinary ⋮ Rapid Review ⋮ Open Access Journal

Received February 6, 2021, accepted February 11, 2021, date of publication February 22, 2021, date of current version March 2, 2021.

Digital Object Identifier 10.1109/ACCESS.2021.3060632

Temperature Rise Test and Thermal-Fluid Coupling Simulation of an Oil-Immersed Autotransformer Under DC Bias

MINGYANG LI[1], ZEZHONG WANG[1], JUNSHUANG ZHANG[2], ZHENGZE NI[1], (Graduate Student Member, IEEE), AND RUIJUAN TAN[3]

[1]State Key Laboratory of Alternate Electrical Power System With Renewable Energy Sources, North China Electric Power University, Beijing 102206, China
[2]State Grid East Inner Mongolia Eastern Power Company Ltd., Hohhot 010010, China
[3]China Electric Power Research Institute Company Ltd., Beijing 100192, China

Corresponding author: Mingyang Li (762504044@qq.com)

This work was supported in part by the National Key Research and Development Program of China under Grant 2016YFC0800100.

ABSTRACT Loss and temperature increase due to DC bias occurring in power transformers may lead to damage and reduced lifespan. To study the influence of different levels of DC bias on the temperature rise in transformer structural components, 0, 8, and 16 A DC were introduced into the MV side of a test transformer. A 2D axisymmetric finite element model was also established to calculate and analyze the distribution of winding loss under DC bias. Combined with the 3D field-circuit coupling model, the core loss under DC bias was calculated on the basis of the half-wave average algorithm. The eddy loss of the steel structure was also obtained using a 3D field-circuit coupling model. On the basis of the thermal-fluid coupling model, the transient temperature changes of typical points were simulated. Results showed that the calculation error of loss and temperature are small when the DC current is 0 A. Moreover, the error of loss and temperature increases when the DC current is 8 or 16 A. The methods used in this study lay the foundation for subsequent research on the temperature rise of large-capacity power transformers under DC bias, especially for the single phase transformers with ONAN cooling mode.

INDEX TERMS DC bias, loss, thermal-fluid coupling, temperature rise.

I. INTRODUCTION

Geomagnetic storms, unipolar asymmetric operation of high voltage direct current (HVDC) transmission projects, and nonlinear power electronic components in the power grid will lead to the flow of DC through the transformer in the power grid, which will cause the DC bias of the transformer. Given the long transmission distance and small resistance of conductors, transformers with higher voltage grade become susceptible to DC bias [1]–[5].

After DC bias, half-wave saturation occurs in the core, and magnetic flux leakage and structural loss increase, which can lead to local hotspots on the structure. In the area seriously affected by magnetic leakage, non-magnetic materials or electromagnetic shielding is used to reduce local loss, and a large margin is reserved in the temperature design to ensure safe and stable operation of the transformer under abnormal conditions such as DC bias.

The associate editor coordinating the review of this manuscript and approving it for publication was Muhammad Zubair.

The winding of transformers is in a nonuniform magnetic field, and winding loss is usually calculated by the analytic approximation method or the finite element method (FEM). For a 10 kW, 0.5/2.5 kV, 1 kHz transformer, the winding loss under different winding layouts is calculated and analyzed on the basis of Dowell's methods [6], [7]. As magnetic field intensity is less distorted in winding designs with a high porosity factor, Dowell's basic equation yields fairly accurate results at medium frequency. However, for special cases, such as DC bias, the core model in the FEM model has an influence on the magnetic field distribution in the winding area, and more accurate results can be obtained by using the FEM method.

For calculating hotspot temperature of structural parts under normal operation of transformers, magnetic-thermal-fluid-coupling method [8]–[10] or heat dissipation coefficient [11] is used. A closed-loop iterative framework was formulated by coupling the analytical model (based on electromagnetic analysis) and CFD (based on thermal-fluid analysis) to address the temperature dependence in reference [7].

The determination of heat dissipation coefficient is difficult, and an inaccurate heat dissipation coefficient causes a large calculation error. Thermal-fluid-coupling simulation should be performed to obtain an more accurate temperature distribution.

Existing literature has focused more on the test and calculation of the transformer winding hot-spot and top oil temperature [12]–[15] and the test of hot-spot temperature rise [16] under DC bias and less on the calculation of hot-spot temperature rise under DC bias. The key and difficulty of temperature rise calculation under DC bias of transformers lie in the accurate loss calculation model and temperature calculation model.

Based on the customized single-phase, four-column autotransformer test model, the temperature rise test under DC bias was performed in this paper. The calculation model of loss and temperature rise of the test transformer was established, and the correctness of the calculation model was verified by comparison with the test results.

II. TEST PLATFORM

Table 1 shows the rated parameters of the single-phase four-column autotransformer studied in this paper. Fig. 1(a) displays the physical diagram of the test transformer. The following studies were all aimed at this test transformer. Fig. 1(b) depicts the connection mode of the inner winding of the transformer. The low-voltage (LV) winding is composed of two parallel coils LV_I and LV_{II}, medium-voltage (MV) winding consists of two parallel coils MV_I and MV_{II}, and high-voltage (HV) winding comprises four parallel coils HV_{I1}, HV_{I2}, HV_{II1}, and HV_{II2}.

TABLE 1. Parameters of the test transformer.

Name	Parameters
Rated capacity (kVA)	5/5/1.8
Rated frequency (Hz)	50
Rated voltage (V)	360/180/60
Rated current (A)	13.9/27.8/30
HV/MV/LV winding turn	63/63/21
DC resistance of HV winding (Ω)	0.083
DC resistance of MV winding (Ω)	0.032
Core structure	2 main columns, 2 side columns
Core joint configuration	Multi-step lap mitred joints

LV_I, MV_I, HV_{I1}, and HV_{I2} were arranged on the core main column I from the inside to the outside. LV_{II}, MV_{II}, HV_{II1}, and HV_{II2} were arranged on the core main column II from the inside to the outside.

Fig. 1(c) shows the circuit diagram of temperature rise test under DC bias. The function of capacitance C in Fig. 1(c) is to prevent the DC entering the power source side.

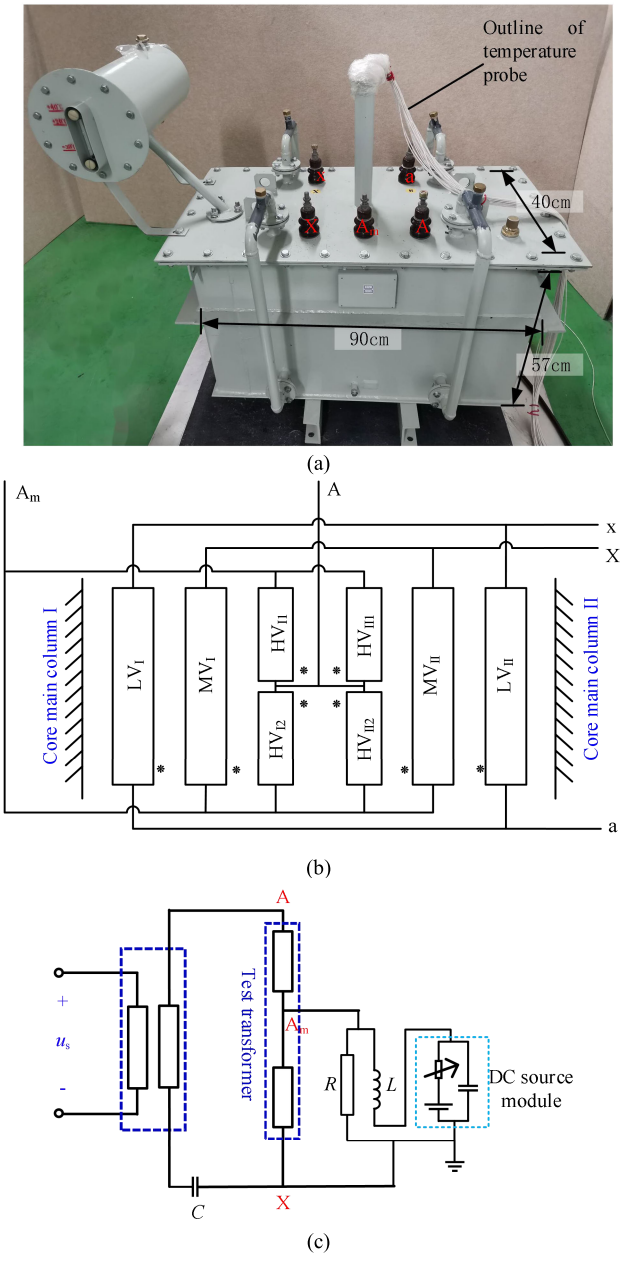

FIGURE 1. Test platform. (a) Physical diagram of the test transformer. (b) Winding connection mode. (c) Test wiring diagram.

In the test and simulation analysis in the following part, the HV side (A-X) applied a rated voltage (u_s), MV side (Am-x) applied a resistance–inductive load (parallel between resistance R and inductance L), and LV side (a-x) applied no load. The DC source was in series with the load inductor L, and DC was introduced from the load side.

Table 2 shows the temperature rise test process. The test can be divided into four test stages lasting for 24 h. To analyze the temperature change caused by different sizes of I_{DC} (DC current), I_{DC} of 0, 8, 16, and 0 A were successively introduced into the MV side of the test transformer. Transitioning from the cold state to the thermal stable state takes a long time;

TABLE 2. Test process.

Stage	Time/hour	Voltage /p.u.	DC/A
1	0-7	1	0
2	7-15	1	8
3	15-22	1	16
4	22-24	0	0

thus, a continuous application of I_{DC} can shorten the total test time.

Fig.2 illustrates the arrangement of temperature measuring points, and Table 3 displays only the measuring points at typical positions. A PT100 temperature sensor was arranged at each measuring point, and the temperature data were collected in a computer every 1 minute by the acquisition equipment. The ambient temperature was measured by PT100 temperature sensors inserted into four 1000 mL suspended metal oil bottles, and the average value was obtained as the ambient temperature.

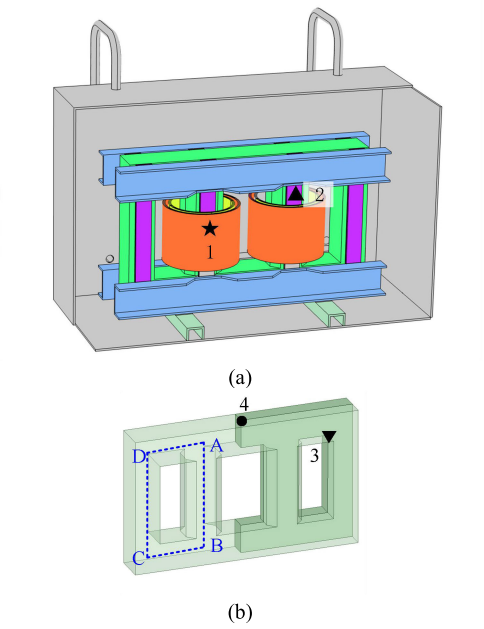

FIGURE 2. Arrangement of temperature measuring points. (a) Partial temperature measuring point arrangement. (b) Arrangement of temperature measuring points on the core surface.

TABLE 3. Temperature sensor number and location description.

Location number	Location description	Symbol
1	HV coil surface	★
2	Top surface of main column tie plate	▲
3	Core surface	▼
4	Core surface	●

The total loss of the transformer and temperature change curve of each measuring point under DC bias were measured. The loss and temperature results are shown in the simulation section below.

III. SIMULATION AND ANALYSIS OF LOSS UNDER DC BIAS

In this section, the loss of each structure under DC bias is calculated, and the correctness of the loss calculation model was verified by comparison with the total loss measured by the test.

A. 3D FIELD-CIRCUIT COUPLING MODEL

The field-circuit coupling (FCCP) method is widely used in the calculation and analysis of DC bias problem of transformers. The circuit model was established on the basis of the actual circuit connection mode of DC bias test (Fig. 3(a)). The 1/4 FEM model was established based on the geometric dimensions and structural symmetry of the test transformer

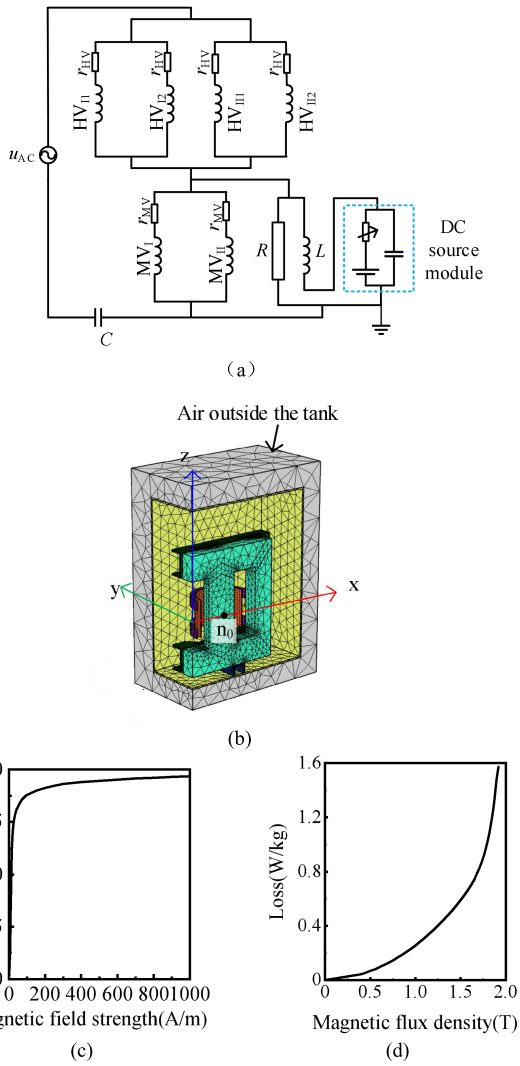

FIGURE 3. Field-circuit coupling model for loss simulation. (a) Circuit model. (b) 1/4 FEM model. (c) *B* - *H* curve of cored silicon steel sheet. (d) *B* - *P* curve of cored silicon steel sheet.

(Fig. 3(b)) (the mesh of transformer oil filled between the structural parts is hidden). The transient magnetic field was simulated based on the FCCP model [17], and the distributions of magnetic field and eddy loss in each structure were obtained.

The boundary conditions of the FEM model were as follows: the magnetic normal boundary condition was applied to the exterior side of faces, where x equals 0 in the model (Fig. 3(b)). And the magnetic parallel boundary condition was applied to the other five outer faces.

The following assumptions were made in the FEM model:

1) The coil was constructed as a block conductor.

2) The material type of core silicon steel sheet was B23R85, and the core block model was constructed. The magnetic properties of the core were characterized by the DC magnetization curves of the silicon steel sheet.

3) The material types of steel structure parts (tie plate, clamp, oil tank and support parts) were Q235A, and the structural parts were subdivided into multilayer mesh considering the skin effect.

B. CORE LOSS

The magnetic flux density waveform of point n_0 in Fig. 3b within a period was extracted, as shown in Fig. 4. In the figure, the magnetic flux density waveform of the core moved up as a whole under DC bias, but its shape is almost unchanged. That is, the waveform is mainly composed of a 50 Hz sinusoidal component and a DC component. In this section, the half-wave average algorithm in references [18], [19] was used to calculate the core loss under DC bias. The main ideas of the half-wave average method are introduced as follows: The part above the x-axis of the waveform of each period is approximated as a sine wave with a frequency of 50 Hz and an amplitude of B_p(at time t_p). The part below the x-axis is approximated as a sine wave with a frequency of 50 Hz and an amplitude of B_b(at time t_b). In the FEM model (Fig. 3(a)), the magnetic flux density B_e of each element in the core was extracted at time t_p; the loss p_e (W/kg) of each element was obtained by interpolating the B–P curve of silicon steel sheet without DC bias (Fig. 3(d)). Then, using (1), core body loss P_{tp} at the time t_p can be obtained. In (1), k_{sym} is the symmetry coefficient (value is 4), ρ is the density of silicon steel sheet (kg/m^3), and V_e is the element volume (m^3). Similarly, the core body loss P_{tb} can be obtained at time t_b. The periodic average body loss P_{core} of the core can be obtained by averaging the losses at time t_p and t_b, as shown in (2). The core loss under different I_{DC} is shown in Table 4.

$$P_{tp} = k_{sym}\rho \sum_{e=1}^{N_e} p_e V_e \tag{1}$$

$$P_{core} = (P_{tp} + P_{tb})/2 \tag{2}$$

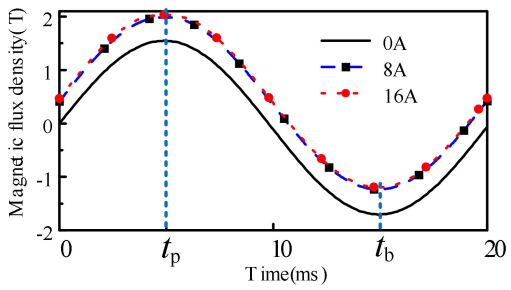

FIGURE 4. The magnetic flux density waveform of n_0 point in one period under different I_{DC}.

C. WINDING LOSS

Numerous harmonic components are involved in the winding current under DC bias. The skin, proximity and edge effects of winding should be considered to obtain an accurate winding loss. The winding loss under DC bias was calculated based on the 2D axisymmetric FEM method. Given the large number of winding turns, the computation cost of winding loss directly based on three-dimensional (3D) FEM model was extremely large. The 3D, four-column structure should be equivalent to the 2D axisymmetric structure to reduce the calculation amount. Fig. 5 shows the geometric model of the 2D axisymmetric structure.

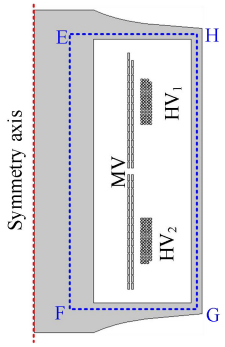

FIGURE 5. Geometric model of 2D axisymmetric structure.

The equivalent method of 2D axisymmetric FEM model is as follows: the length and cross-sectional area of E–F, F–G, G–H, and H–E segments of 2D model are equal to those of A–B, B–C, C–D, and D–A respectively in the 3D model (Fig. 2 (b)). Similar to the simulation method of 3D FCCP model, the winding current under DC bias can be obtained based on the 2D axisymmetric FEM model. Fig. 6 shows the comparison of the winding current under I_{DC} of 16 A. Fig. 6 also reveals that the winding current waveforms obtained by 2D axisymmetric FEM model and 3D FCCP model were in good agreement with the measured winding current waveforms, thus verifying the correctness of the 2D axisymmetric FEM model.

Fig. 7(b) displays the magnetic flux density (B) vector line distribution and the winding conductor loss contour distribution of 2D axisymmetric FEM model at time t_p. Fig. 7 shows that the conductor at the end of the coil was greatly affected by transverse magnetic flux leakage, and the internal loss distribution of each turn of conductor was uneven.

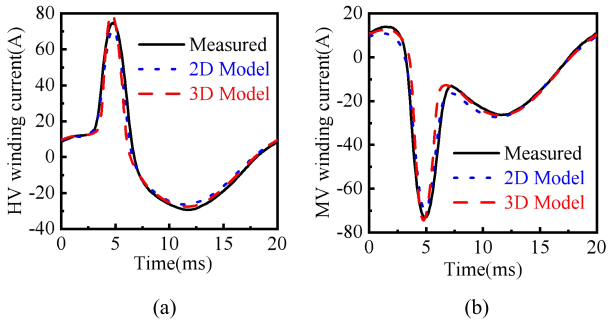

FIGURE 6. Comparison of winding current under I_{DC} of 16 A. (a) HV winding current. (b) MV winding current.

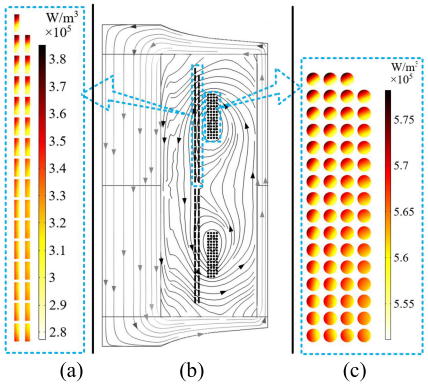

FIGURE 7. Distribution of B vector line and wire loss at time t_p under I_{DC} of 16 A. (a) Loss distribution of partial MV coil conductor at time t_p. (b) B vector line distribution at time t_p. (c) Loss distribution of HV_1 coil conductor at time t_p.

Based on the 2D axisymmetric FEM model, the average body loss of windings under different I_{DC} was calculated (Table 4).

D. STRUCTURAL PART LOSS

The material type of the steel structure parts (tie plate, clamp, oil tank, and support parts) of the test transformer is Q235A. Q235A has a nonlinear magnetization characteristic curve. The losses of steel structure with irregular shape in time-varying magnetic field mainly includes eddy loss and hysteresis loss. Under DC bias, the saturation of the core, the magnetic flux leakage, and the loss of the steel structure increase. The 3D FCCP model shown in Fig. 3 was also used to simulate the eddy loss of steel structure. Given that the current mainstream electromagnetic field FEM software cannot simulate the hysteresis loss of the steel structure under DC bias, this study does not calculate the hysteresis loss of the steel structure and only calculates the eddy loss of the steel structure.

Table 4 summarizes the calculated periodic average body loss of each structure.

As shown in Table 4, the relative errors of total loss between the simulation and test values under I_{DC} of 0, 8, and 16 A were 3%, 4%, and 8%, respectively. When no DC bias was present, the calculation error of the total loss, which mainly consisted of winding and core losses, was small. The losses in the core, main column tie plate, and winding increased under DC bias. At the same time, the proportion of hysteresis loss in the total loss increases. At this point, ignoring the hysteresis loss of the steel structure leads to the increase in the error of the total loss and the increase in the calculation error of the temperature in section IV.

Given that the total loss is measured in the test, the loss of each substructure cannot be separated; thus, the calculation accuracy of the loss of each substructure cannot be analyzed in detail.

TABLE 4. Periodic average body losses.

Structure	I_{DC} = 0A	I_{DC} = 8A	I_{DC} = 16A
HV winding (W)	13.26	26.75	47.41
MV winding (W)	5.93	9.89	22.26
Core (W)	54.66	81.69	83.35
Main column tie plate (W)	0.38	28.09	77.05
Side column tie plate (W)	8.21e-4	8.22e-3	6.37e-2
Clamp (W)	0.02	1.09	2.56
Tank (W)	2.93e-3	3.90e-2	0.10
Support structure (W)	3.66e-4	3.99e-3	9.63e-3
Total loss - calculated value (W)	74.26	147.57	232.80
Total loss - tested value (W)	72.00	154.00	254.00
Total loss - relative error	0.03	0.04	0.08

IV. SIMULATION AND ANALYSIS OF TEMPERATURE DISTRIBUTION UNDER DC BIAS

In this section, a 3D thermal-fluid coupling (TFCP) model is established on the basis of FEM software to simulate and analyze the transient temperature change of each measuring point.

A. FLOW STATE ESTIMATION

The flow state, fluid-momentum-boundary-layer thickness and fluid velocity of transformer oil must be estimated first to select a suitable fluid-field-calculation method and establish an accurate fluid-field-calculation model. The cooling mode of the test transformer in this paper is oil natural–air natural. Buoyancy was generated by heating the transformer oil, which drove the flow of oil. The velocity and temperature gradient of the fluid varied greatly in the momentum boundary layer. The distance from the surface of the structure to the peak value of oil flow velocity can be estimated using the momentum boundary layer thickness δ_M. When defining the fluid FEM mesh, the mesh within δ_M must be refined, for example, inserting three to five elements within δ_M.

The expression of δ_M is shown in (3), where u is the estimated typical velocity of fluid (Equation (4)), R_a is Rayleigh number (Equation (5); a dimensionless number), and G_r

is Glasshoff number (Equation (6)). L is the characteristic dimension of the structure surface, g is the acceleration of gravity, and β is the thermal expansion coefficient of transformer oil. ΔT is the temperature difference between the surface temperature T_w of structural parts and temperature T_o of transformer oil. k, v, C_p, and ρ are the thermal conductivity, viscosity, specific heat capacity, and density of transformer oil, respectively. The thermal property parameters of transformer oil were calculated at a temperature of $(T_w + T_o)/2$.

$$\delta_M \approx \frac{L}{\sqrt{\frac{\rho u L}{v}}} \tag{3}$$

$$u = \frac{k}{\rho C_p L}\sqrt{R_a} \tag{4}$$

$$R_a = \frac{c_p L_1^3 g\beta\rho^2\Delta T}{kv} \tag{5}$$

$$G_r = \frac{L_1^3 g\beta\rho^2\Delta T}{v^2} \tag{6}$$

The thermal property parameters of the transformer oil (k, υ, C_p, and ρ) vary with temperature (Table 5).

TABLE 5. Thermal properties of transformer oil.

Thermal property names	Fitting formula
Density (kg/m^3)	ρ = 1055.04-0.58T-6.41e-5T^2
Viscosity (Pa·s)	υ = 14.98-0.12T-2e-4 T^2
Thermal conductivity (W/(m·K))	k = 0.134-8.049e-5T
Specific heat capacity (J/(kg·K))	C_p = 807.16+3.58T

We set L at 0.386 m (core height) and T_o at 10°C; the ranges of δ_M, u, and Gr were calculated in accordance with (3), (4), and (6), respectively, when ΔT changed from 0°C to 20°C (Fig. 8). The physical values calculated here are estimates of the order of magnitude. G_r is used to assess the flow situation for natural convection. Flow can be regarded as laminar flow when G_r is less than 1e9.

Fig. 8 shows that G_r and u increased, whereas δ_M decreased with the increase in temperature difference. Throughout the temperature range, δ_M was greater than 0.02 m, u was less than 0.02 m/s, and G_r was less than 1e9 (transformer oil flow was laminar).

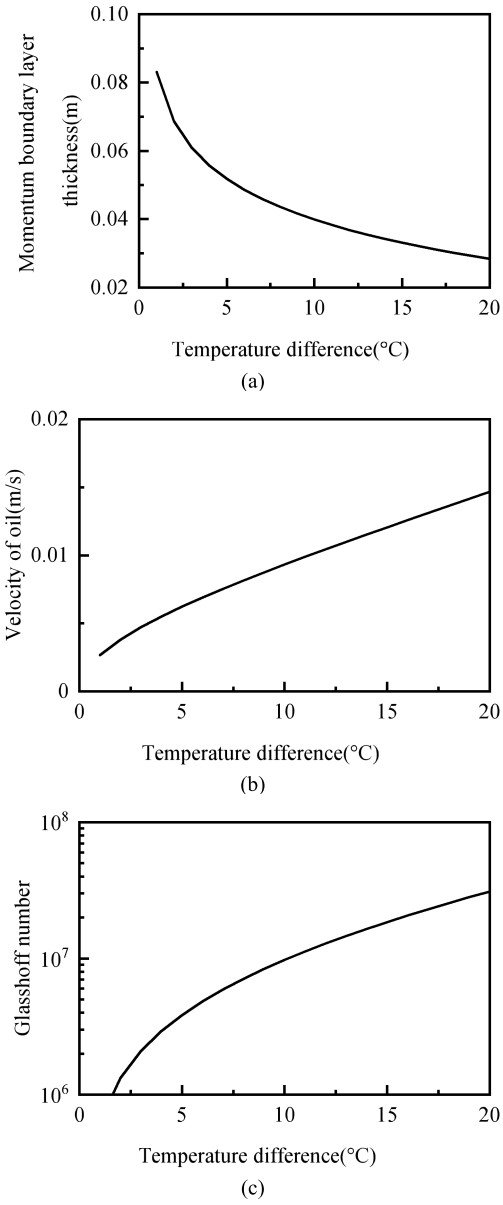

FIGURE 8. Estimation of transformer oil flow parameters at different temperature differences. (a) Momentum boundary layer thickness. (b) Velocity of oil. (c) Glasshoff number.

B. THERMAL–FLUID COUPLING MODEL

The 1/4 TFCP model was established based on symmetry (Fig.9). In the model, the x = 0 and y = 0 faces were set as symmetric boundaries. The top of the oil pillow tube in Fig. 9 was set as an open boundary to simulate the expansion or contraction of the oil volume with the temperature change.

Based on the method mentioned in III.B, the loss of each element of the core under DC bias can be obtained. The file containing the coordinates of the center point of each element and the loss of each element can be extracted. Given that the mesh of the FEM model for the thermal-fluid coupling calculation differs from that of the FEM model for the loss calculation mentioned above, after the loss file was imported into the TFCP model, the FEM software was used to obtain the heat source distribution by interpolating the spatial coordinates.

Given the small size of coils and tie plates of the test transformer and the relatively uniform loss distribution, the losses were assumed to be uniformly distributed in the coils and tie plates. The uniform loss density can be obtained by dividing loss by volume.

The air outside the oil tank was not established in the TFCP model to reduce the computational scale. Instead, the radiation rate of the outer surface of the tank was given the equivalent of thermal radiation effect of the tank surface on the

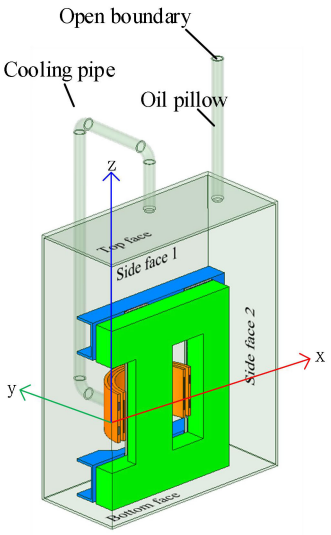

FIGURE 9. The 1/4 FEM model for thermal-fluid coupling calculation.

environment. The calculation formula of the heat dissipation coefficient of the external surface of the oil tank was given an equivalent of the cooling effect of air flow on the oil tank. The ambient temperature in the simulation was set to be the same as that measured by the previous temperature rise test.

The mathematical description of thermal radiation is shown in (7), where q is the radiated heat, ε is the emissivity of the oil tank surface, A is the radiation area, σ is the blackbody radiation constant, T_{tank} is the surface temperature of the oil tank, and T_{amb} is the ambient temperature.

$$q = \varepsilon A\sigma \left(T_{\tan k}^4 - T_{\text{amb}}^4\right) \tag{7}$$

The four outer surfaces of the tank in contact with air in the 1/4 FEM model were respectively recorded as "Bottom face," "Side face 1," "Side face 2," and "Top face" (Fig. 9). The average surface heat dissipation coefficient of "Side surface 1" and "Side surface 2" (vertical wall) of the oil tank is shown in (8) [20], where the characteristic length L_1 is the height of oil tank.

$$h_1 = \frac{k}{L_1}\left[0.825 + 0.387R_a^{1/6} \Big/ \left(1 + \left(\frac{0.492k}{\nu C_p}\right)^{\frac{9}{16}}\right)^{\frac{8}{27}}\right]^2 \tag{8}$$

The average surface heat dissipation coefficient of the "Top face" of the oil tank is shown in (9)[20]], where the characteristic length L_2 is the ratio of the area to the perimeter of the "Top face."

$$h_2 = \begin{cases} \dfrac{k}{L_2}0.54R_a^{1/4}, \left(10^4 \le R_a \le 10^7\right) \\ \dfrac{k}{L_2}0.15R_a^{1/3}, \left(10^7 \le R_a \le 10^{11}\right) \end{cases} \tag{9}$$

The average surface heat dissipation coefficient of the "Bottom face" of the oil tank is shown in (10) [20], where the characteristic length L_3 is the ratio of the area to the perimeter of the "Bottom face."

$$h_3 = \frac{k}{L_3}0.27R_a^{1/4}, \left(10^5 \le R_a \le 10^{10}\right) \tag{10}$$

The heat dissipation coefficients h_1, h_2, and h_3 of the outer surface of the oil tank changed with temperature. The FEM software considers the heat dissipation coefficient as one of the unknown variables to calculate the temperature field.

Table 6 shows the thermal property parameters of each structure of the test transformer.

TABLE 6. Thermal property parameters of each structure.

Structure name	Density (kg/m^3)	Specific heat capacity (J/kg*K)	Thermal conductivity (W/m*K)	
Core	7650	485	Parallel to silicon steel sheet	21
			Perpendicular to the silicon steel sheet	3.3
Clamp, Tie plate	7850	485	50	
Copper	8890	390	350	
Insulating board	1100	2000	0.25	

C. TEMPERATURE SIMULATION RESULTS AND COMPARATIVE ANALYSIS

Based on the TFCP model, the transient temperature of each position was obtained by simulation. Fig. 10 gives the comparison between the simulation and measured values of the transient temperature of each measuring point.

As shown in Fig. 10, after DC bias, the temperature of each measuring point increased rapidly at first and then slowed down; the results under I_{DC} of 0 and 8 A exhibited a smaller error between the simulated results and the experimental findings. Given that the total loss of simulation under 16 A DC bias was lower than the actual total loss of measurement, the simulation temperature of each measuring point under 16 A DC bias was lower than the test temperature.

The velocity vector diagram on the symmetrical plane at 22 h was obtained by simulation (Fig. 11). As shown in Fig. 11, the oil moved upward, driven by buoyancy after heating, but moved downward after cooling by the tank wall. The maximum velocity of oil was approximately 1.5 cm/s, which is in accordance with the order of magnitude of the estimated value in (4). The oil flow velocity near the top of the core and the tank wall was higher than that in other locations.

The cloud diagram of temperature distribution at 22 h was obtained by simulation (Fig. 12). As shown in Fig. 12, the middle position of the upper surface of the yoke of the core and the temperature of the main tie plate were high. The maximum and minimum temperatures of the surface of the structure were 29.9°C and 19.6°C, respectively.

The heat flux cloud image of the structure surface at 22 h was obtained by simulation (Fig.13). Fig. 13 shows that the heat flux cloud diagram is similar to the temperature distribution cloud diagram, and the heat flux is large where the temperature is high.

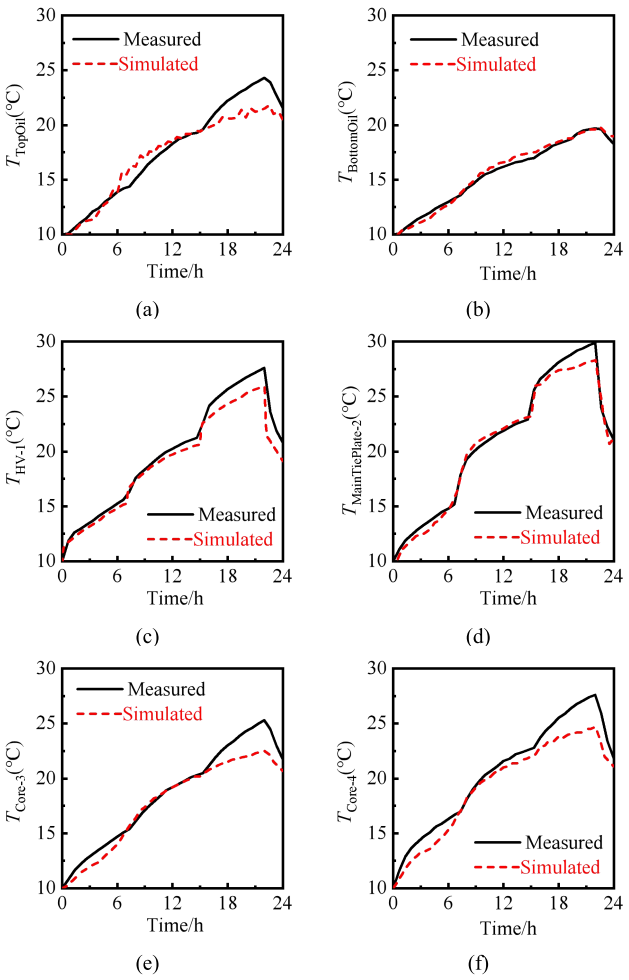

FIGURE 10. Transient temperature comparison. (a) Temperature of top oil. (b) Temperature of bottom oil. (c) Temperature of HV coil surface (measuring point 1). (d) Temperature of main column tie plate surface (measuring point 2). (e) Temperature of core surface (measuring point 3). (f) Temperature of core surface (measuring point 4).

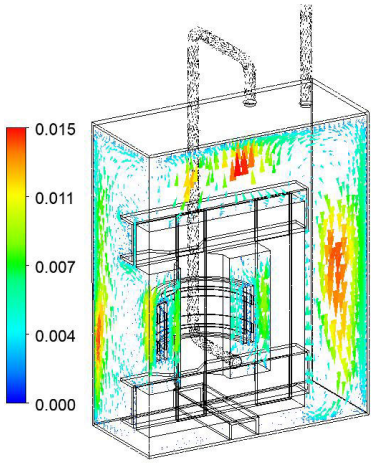

FIGURE 11. Velocity vector diagram on the symmetrical plane at 22 h (m/s).

V. DISCUSSION OF RESULTS

In this study, the loss of each structure and the transient temperature of typical measuring points under DC bias are calculated. The main calculation methods used in this study and the results are discussed below.

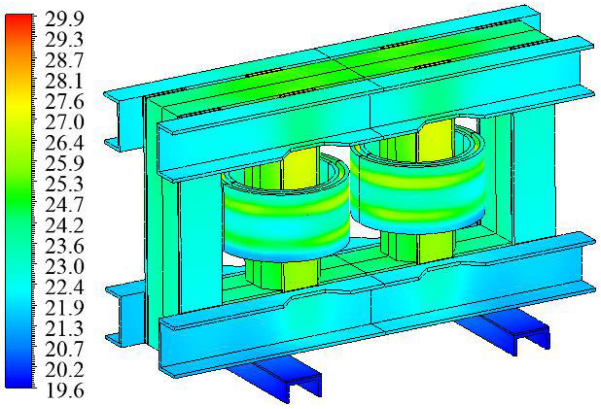

FIGURE 12. Cloud diagram of temperature at 22 h (°C).

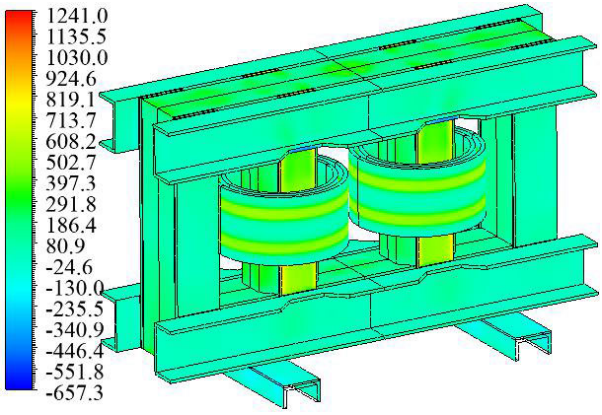

FIGURE 13. Heat flux cloud diagram at 22 h (W/m^2).

A 2D axisymmetric FEM model is used to calculate the winding loss in this study. This model can simulate the influence of core saturation to obtain more accurate results. Moreover, the method can be easily extended to calculate the winding loss of large-capacity transformers.

The half-wave average method is used to calculate the core loss under DC bias in this study. To use this method, the magnetic field distribution in the core and the $B - P$ curve of the silicon steel sheet under normal conditions are used. The magnetic field distribution in the core can be obtained by the 3D FCCP model, and the $B-P$ curve of the silicon steel sheet can usually be obtained from the manufacturer. Therefore, the half-wave average method can be easily applied to the calculation of the core loss of large-capacity transformers under DC bias.

For small-capacity power transformers, the steel structure parts (tie plate, clamp, and oil tank) mostly use a magnetic steel plate. For large-capacity power transformers, nonmagnetic steel plates are often used in the tie plate near the core, and electromagnetic shielding is installed in the area with serious magnetic leakage. The loss in magnetic steel plate mainly includes eddy loss and hysteresis loss. Current

mainstream FEM software cannot calculate the hysteresis loss of steel structures with irregular shape under DC bias. The calculation of hysteresis loss of steel structure needs further study to improve the calculation accuracy.

On the basis of the TFCP model, the transient temperature of typical points is calculated and analyzed. Compared with the temperature distribution under a steady state, the comparison of transient temperature can better illustrate the correctness of the model.

The cooling structure inside the winding and the structure of the external cooler of large-capacity power transformers are more complex than that of small-capacity power transformers; thus, the TFCP model of large-capacity transformers is much more complex than the model in this study.

VI. CONCLUSION

This study calculates and analyzes the loss and temperature variation of single-phase four-column test transformer models under DC bias. When no DC bias occurs, the calculation model in this study can obtain more accurate loss and temperature results.

After DC bias, the winding current waveform is distorted, the half-wave saturation occurs in the core, the magnetic flux leakage increases, and the loss of all structures increases. In this study, the winding loss under DC bias is calculated on the basis of the 2D axisymmetric FEM model, the core loss under DC bias is calculated on the basis of the half-wave average method, and the eddy loss of steel structure under DC bias is calculated on the basis of the 3D FCCP model. After DC bias, the loss of the core, main tie plate, and winding increase substantially. The relative errors of total loss under a DC bias of 0, 8, and 16 A are 3%, 4%, and 8%, respectively.

With the loss results taken as the heat source of the TFCP model, the transient temperatures of typical points are calculated and analyzed. After DC bias, the temperature of the core, main tie plate, and winding increase substantially. When no DC bias occurs, the error between the simulation and experimental results is small, verifying the correctness of the TFCP model. The increase in the error of temperature calculation results at 8 and 16 A is due to the loss calculation error.

Online condition monitoring interfaced with dynamically controlled transformer cooling could be used to detect and mitigate the potential temperature increase in large-capacity transformers due to DC bias.

REFERENCES

[1] C. Liu, Y. S. Ganebo, H. Wang, and X. Li, "Geomagnetically induced currents in ethiopia power grid: Calculation and analysis," *IEEE Access*, vol. 6, pp. 64649–64658, 2018.

[2] C.-M. Liu, L.-G. Liu, and R. Pirjola, "Geomagnetically induced currents in the high-voltage power grid in China," *IEEE Trans. Power Del.*, vol. 24, no. 4, pp. 2368–2374, Oct. 2009.

[3] L. Marti, J. Berge, and R. K. Varma, "Determination of geomagnetically induced current flow in a transformer from reactive power absorption," *IEEE Trans. Power Del.*, vol. 28, no. 3, pp. 1280–1288, Jul. 2013.

[4] A. Rezaei-Zare, "Behavior of single-phase transformers under geomagnetically induced current conditions," *IEEE Trans. Power Del.*, vol. 29, no. 2, pp. 916–925, Apr. 2014.

[5] N. Takasu, T. Oshi, F. Miyawaki, S. Saito, and Y. Fujiwara, "An experimental analysis of DC excitation of transformers by geomagnetically induced currents," *IEEE Trans. Power Del.*, vol. 9, no. 2, pp. 1173–1182, Apr. 1994.

[6] A. K. Das, H. Tian, Z. Wei, S. Vaisambhayana, S. Cao, A. Tripathi, and P. C. Kjær, "Accurate calculation of winding resistance and influence of interleaving to mitigate ac effect in a medium-frequency high-power transformer," in *Proc. Asian Conf. Energy, Power Transp. Electrific. (ACEPT)*, Oct. 2017, pp. 1–6.

[7] H. Tian, Z. Wei, S. Vaisambhayana, M. Thevar, A. Tripathi, and P. Kjær, "A coupled, semi-numerical model for thermal analysis of medium frequency transformer," *Energies*, vol. 12, no. 2, p. 328, Jan. 2019.

[8] F. Farahmand, F. P. Dawson, and J. D. Lavers, "Temperature rise and free-convection heat-transfer coefficient for two-dimensional pot-core inductors and transformers," *IEEE Trans. Ind. Appl.*, vol. 45, no. 6, pp. 2080–2089, Nov./Dec. 2009.

[9] C. Liao, J. Ruan, C. Liu, W. Wen, and Z. Du, "3-D coupled electromagnetic-fluid-thermal analysis of oil-immersed triangular wound core transformer," *IEEE Trans. Magn.*, vol. 50, no. 11, pp. 1–4, Nov. 2014.

[10] H. Wang, Q. Yang, Y. Li, J. Wang, and Y. Zhao, "Numerical calculation and experimental verification for leakage magnetic field and temperature rise of transformer core tie-plate," *IEEE Trans. Appl. Supercond.*, vol. 29, no. 2, pp. 1–5, Mar. 2019.

[11] L. Li, S. Niu, S. L. Ho, W. N. Fu, and Y. Li, "A novel approach to investigate the hot-spot temperature rise in power transformers," *IEEE Trans. Magn.*, vol. 51, no. 3, pp. 1–4, Mar. 2015.

[12] M. Djamali and S. Tenbohlen, "Hundred years of experience in the dynamic thermal modelling of power transformers," *IET Gener., Transmiss. Distrib.*, vol. 11, no. 11, pp. 2731–2739, Aug. 2017.

[13] D. Susa, M. Lehtonen, and H. Nordman, "Dynamic thermal modelling of power transformers," *IEEE Trans. Power Del.*, vol. 20, no. 1, pp. 197–204, Jan. 2005.

[14] D. Susa, J. Palola, M. Lehtonen, and M. Hyvarinen, "Temperature rises in an OFAF transformer at OFAN cooling mode in service," *IEEE Trans. Power Del.*, vol. 20, no. 4, pp. 2517–2525, Oct. 2005.

[15] G. S. SwiftT Molinski and W. Lehn, "A fundamental approach to transformer thermal modeling. I. Theory and equivalent circuit," *IEEE Trans. Power Del.*, vol. 16, no. 2, pp. 171–175, Apr. 2001.

[16] P. Picher, L. Bolduc, A. Dutil, and V. Q. Pham, "Study of the acceptable DC current limit in core-form power transformers," *IEEE Trans. Power Del.*, vol. 12, no. 1, pp. 257–265, Jan. 1997.

[17] B. Li, Z. Wang, S. Guo, and M. Li, "No load simulation and downscaled experiment of UHV single-phase autotransformer under DC bias," *IEEE Access*, vol. 8, pp. 38872–38879, 2020.

[18] Y. Dang, X. Zhang, J. Ma, N. Dai, and D. Chen, "Calculation of excitation current and core loss of transformer under DC bias," *Transformer*, vol. 56, no. 10, pp. 1–6, Oct. 2019.

[19] J. Ma, W. Liu, H. Li, Q. Chen, and J. Ye, "Influence of DC bias on no-load loss of converter transformer," *Transformer*, vol. 53, no. 1, pp. 35–40, Jan. 2016.

[20] T. Bergman and A. Lavine, *Fundamentals of Heat and Mass Transfer*. Hoboken, NJ, USA: Wiley, 2007.

MINGYANG LI was born in Henan, China, in 1991. He received the B.Eng. degree in electrical engineering and automation from the Institute of Disaster Prevention Science and Technology, Hebei, China, in 2013, and the M.Sc. degree in electrical theory and new technology from North China Electric Power University, Beijing, China, in 2016, where he is currently pursuing the Ph.D. degree in electrical engineering.

His research interests include electromagnetic field numerical calculation and electromagnetic compatibility.

ZEZHONG WANG was born in Shandong, China, in 1960. He received the B.Eng., M.Eng., and Ph.D. degrees from Tsinghua University, in 1983, 1986, and 1989, respectively, all in electrical engineering.

He is currently a Professor and a Doctoral Supervisor with the School of Electrical and Electronic Engineering, North China Electric Power University. His research interests include electromagnetic field numerical analysis, electromagnetic compatibility, and electromagnetic measurement.

JUNSHUANG ZHANG was born in Heilongjiang, China, in 1986. He is currently a Senior Engineer in the field of power equipment detection and diagnosis technology.

ZHENGZE NI (Graduate Student Member, IEEE) was born in Shanxi, China, in 1998. He received the B.Eng. degree from North China Electric Power University, Hebei, China, in 2019. He is currently pursuing the M.Eng. degree in electrical engineering with North China Electric Power University, Beijing, China.

His research interests include electromagnetic field numerical calculation and geomagnetic storm analysis.

RUIJUAN TAN was born in Shandong, China, in 1988. She received the Ph.D. degree in power system and automation from North China Electric Power University, Beijing, China, in 2017.

She engaged in the postdoctoral research for two years with Tsinghua University, Beijing. She is currently an Engineer with the Department of High Voltage, China Electric Power Research Institute. Her research interests include electromagnetic field numerical calculation and short circuit resistance analysis.